International Journal of Science and Research Archive
eISSN: 2582-8185
Cross Ref DOI: 10.30574/ijsra
Journal homepage: https://ijsra.net/

(REVIEW ARTICLE)

Check for updates

Analysis of dual active bridge-based on-board battery charger for electric and hybrid vehicles

Hamed Eyvazi [1,*], Zahra Alimohammadi [2], Ahmad Sheikhi [2], Yaser Adelighalehtak [2] and Touhid Poursheykh Aliasghari [3]

[1] *Department of Electrical and Computer Engineering, University of Catania, Catania, Italy.*
[2] *Department of Electrical and Computer Engineering, University of Pavia, Pavia, Italy.*
[3] *School of Industrial and Information Engineering, Politecnico di Milano, Milan, Italy.*

International Journal of Science and Research Archive, 2024, 12(01), 216–230

Publication history: Received on 23 March 2024; revised on 01 May 2024; accepted on 04 May 2024

Article DOI: https://doi.org/10.30574/ijsra.2024.12.1.0768

Abstract

This paper presents an in-depth analysis of a Gallium Nitride (GaN) Dual Active Bridge (DAB)-based on-board battery charger for electric and hybrid vehicles. It focuses on the superior efficiency and reliability of GaN-based power electronics over traditional Silicon-based systems. The study explores the implementation of the DAB topology, recognized for its bidirectional power flow and high efficiency, in enhancing vehicle charging infrastructure. Efficiency analysis, switching behavior and losses are thoroughly examined. Simulation results in PSIM software validate the theoretical predictions, showing significant improvements in operational flexibility and energy efficiency.

Keywords: Gallium Nitride; Dual Active Bridge; On-board battery charger; Electric vehicles; Power electronics

1. Introduction

In the rapidly evolving landscape of electric and hybrid vehicles (EVs and HVs), the efficiency and reliability of charging systems have become critical factors in advancing automotive technology and promoting wider adoption of these eco-friendly transportation modes. Among the myriad of technologies being explored, Gallium Nitride (GaN) based power electronics have emerged as a ideal innovation, offering superior performance characteristics compared to traditional Silicon-based systems [1-5]. The on-board battery charger is a cornerstone component of EVs and HVs, dictating the vehicles' charging speed, energy efficiency, and operational flexibility. The Dual Active Bridge topology (DAB), renowned for its bidirectional power flow capability and high efficiency, provides an ideal framework for exploiting GaN's high switching frequency, low on-resistance, and exceptional thermal performance. This analysis aims to unravel the technical intricacies and potential benefits of integrating GaN technology into DAB chargers, focusing on aspects such as efficiency improvements, power density, thermal management, and the impact on the vehicle's overall charging infrastructure.

In addition, the conversion of electrical energy plays a key role in many aspects of modern society, from consumer electronics to high-power applications [6]. In the latter case, efficiency, harmonic quality, power density demands, among other requirements, have triggered the development of advanced electronic adjustable-speed drives (ASDs) and sophisticated power semiconductors. More precisely, the use of medium-voltage (MV)-ASDs has been a key technology for high-power applications such as fans, pumps, conveyor belts, propellers, crushers, photovoltaic systems, wind turbines, static compensators, and so on. Further improvements in power semiconductor and converter technologies have allowed the replacement of load-commutated inverters (LCIs), which are still used for output powers in the tens-of-megawatt range, with self-commutated converters. The increased demand for intermediate storage of electrical

* Corresponding author: Hamed Eyvazi

energy in battery systems, particularly due to the use of renewable energy, has resulted in the need for bidirectional DC/DC power converters with galvanic isolation [7-8]. Uninterruptible Power Supplies (UPS), battery charging systems [9], photovoltaic systems [10-14], and auxiliary power supplies in traction applications are examples of some fields of application of this kind of converter. A Dual Active Bridge (DAB) bidirectional DC/DC converter is a topology with the advantages of fewer devices, soft-switching commutations [15-16], low cost, and high efficiency. The use of this topology is proposed for applications where power density, cost, weight, and reliability are critical factors. In the present paper, the steady-state analysis of the DAB converter has been carried out, providing some guidelines for design (considering soft switching and the amount of RMS current) and modulation techniques for DAB topology are discussed with providing simulations results in PSIM.

2. Dual-Active-Bridge Topology, and its Modulations

The two-level dual-active bridge is a bidirectional and controllable DC-DC converter with substantial power capabilities [17]. Figure 1 shows the structure of DAB with eight semiconductor devices, a high-frequency transformer, an energy transfer inductor, and DC-link capacitors where the converter resembles a more common full bridge with a controllable rectifier. Its symmetrical design, featuring identical primary and secondary bridges, enables bidirectional power flow control. The interconnected full bridges, linked by a high-/medium-frequency transformer for galvanic isolation, facilitate power transfer through the transformer's leakage inductance. Controlled switching actions generate square voltages namely V_{T1} and V_{T2} on both sides, enhancing efficiency compared to hard-switched topologies. This design achieves higher switching frequencies without excessive losses, particularly with soft switching.

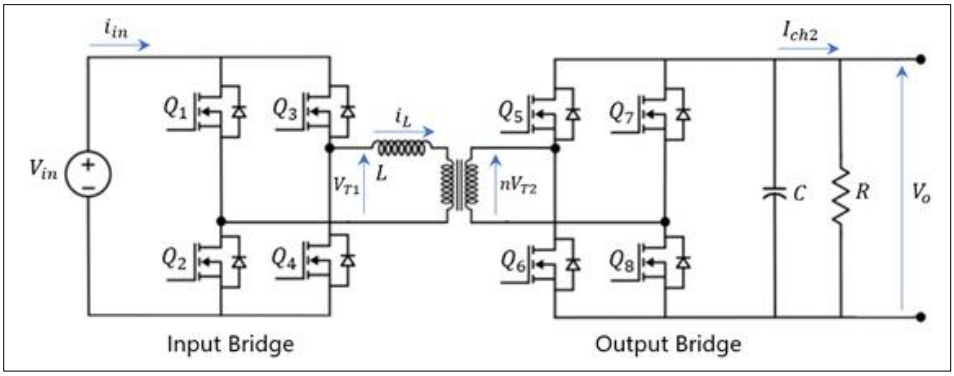

Figure 1 The structure of dual active bridge

At elevated frequencies, the isolation transformer's magnetizing inductance diminishes, simplifying the model to its leakage inductance and reducing weight for easier transport. Figure 2 illustrates an equivalent system used to derive the power equation. Additionally, the dual-active bridge's bidirectional nature makes it suitable for energy storage applications, such as linking batteries in automotive use [18-19].

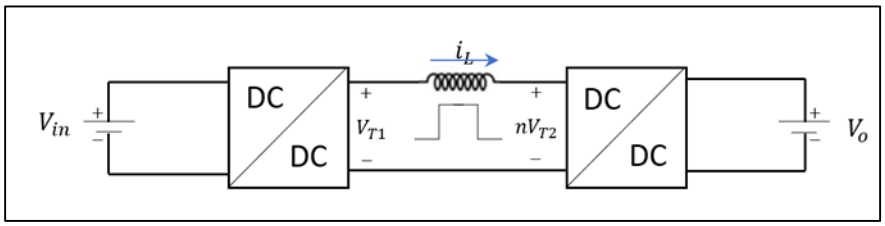

Figure 2 The equivalent circuit of dual active bridge in high frequencies

There are various modulation techniques for DAB converters including single-phase-shift (SPS) control, dual-phase-shift control, extended-phase-shift control, triple-phase-shift control, as well as trapezoidal, triangular, and optimized modulation methods. The single-phase-shift modulation and the trapezoidal modulation scheme are chosen for modeling, simulation, and testing in PSIM® software. In a DAB converter, three parameters affect power flow between primary and secondary sides: phase-shift between square voltages, duty cycle of square voltages, and switching frequency [20-21]. The modulation techniques considered here involve changes in phase-shift and/or duty cycle to control power flow, while frequency switching methods are excluded from consideration in this study. The single-phase-shift modulation only uses a phase shift between the two transformer voltages to control the power flow, while the

trapezoidal modulation uses a phase shift and additionally changes the duty ratio of the transformer voltages, introducing a zero-voltage period. The zero-voltage period is attained by introducing a phase shift between the two legs of each full bridge [22].

2.1. Single-Phase-Shift Modulation

The SPS control is the standard modulation scheme for the DAB and describes a classical method to implement a voltage-controlled DC-to-DC converter. The method is easy to implement and shows excellent control performance, but the overall efficiency is not sufficient. The square voltages in a circuit that is modulated with this scheme will always have duty cycles of 50% of the switching period while the frequency stays constant [23]. Two square voltages V_{T1} and nV_{T2} are generated on the primary and secondary side of the transformer by giving respective switching signals to the switches Q_1 to Q_8. A phase-shift φ is introduced between the switching signals for the primary side and the switching signals for the secondary side, leading to the same phase-shift φ between the two voltages V_{T1} and nV_{T2}. A voltage difference is induced and a current flow from the primary to the secondary side. This is shown in Figure 3. There are four commutation states of the power switches to achieve the SPS modulation method which are shown in Figure 4 and Table1.

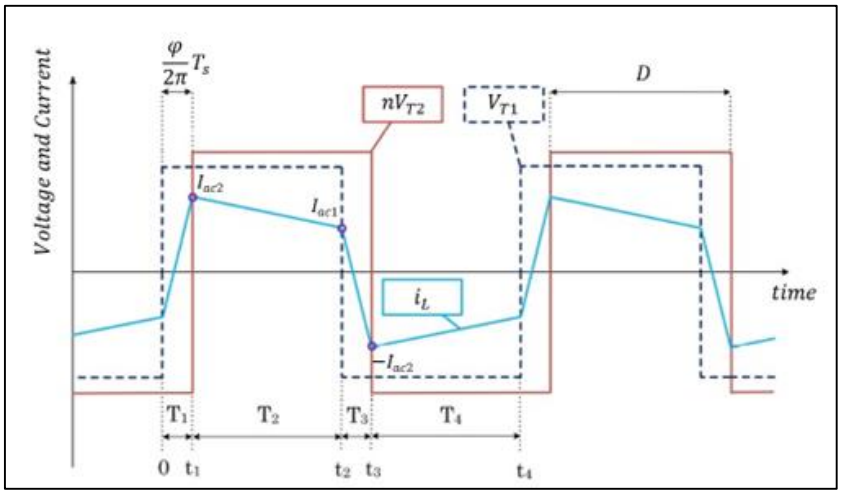

Figure 3 Primary and referred secondary transformer voltage and inductor current for the single-phase-shift modulation

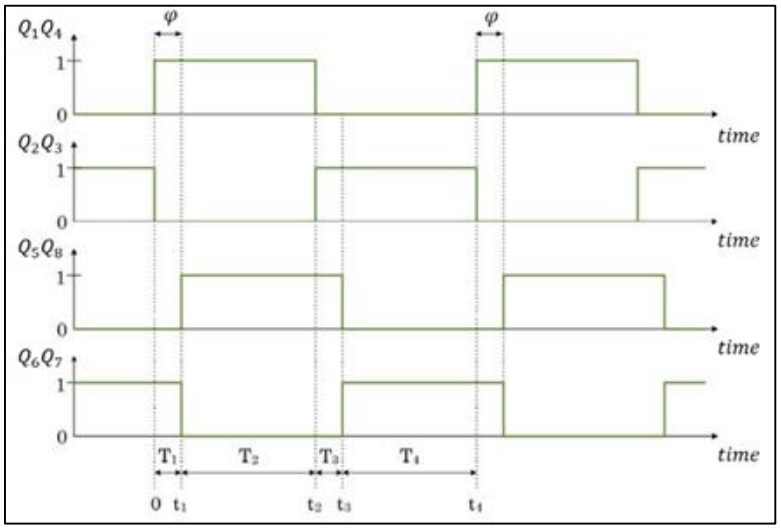

Figure 4 Switching signals for the gates Q_1 to Q_8

Table 1 Commutation sequence of switches for the SPS modulation

Q_1	Q_2	Q_3	Q_4	Q_5	Q_6	Q_7	Q_8	V_{T1}	nV_{T2}	**Duration**
1	0	0	1	0	1	1	0	$+V_{T1}$	$-nV_{T1}$	T_1
1	0	0	1	1	0	0	1	$+V_{T1}$	$+nV_{T1}$	T_2
0	1	1	0	1	0	0	1	$-V_{T1}$	$+nV_{T1}$	T_3
0	1	1	0	0	1	1	0	$-V_{T1}$	$-nV_{T1}$	T_4

2.2. Trapezoidal Modulation

Equal to the single-phase-shift modulation [24], the two transformer voltages will be phase-shifted in the trapezoidal modulation scheme. In addition to that, two inner phase shifts are introduced between the two legs of each full bridge. This causes the duty cycle of and to change and introduces a period during which and will be zero [25]. These intervals are named ω_1 and ω_2 can be seen in Figure 5. It is notable that the on and off times of the switches continue to equal 50% of one switching period, and it is only the duty cycles of the transformer voltages that change. There are eight commutation states of the power switches to achieve the trapezoidal modulation method which are shown in Figure 6 and 7. Commutation sequence of switches for the Trapezoidal modulation is tabulated in Table 2.

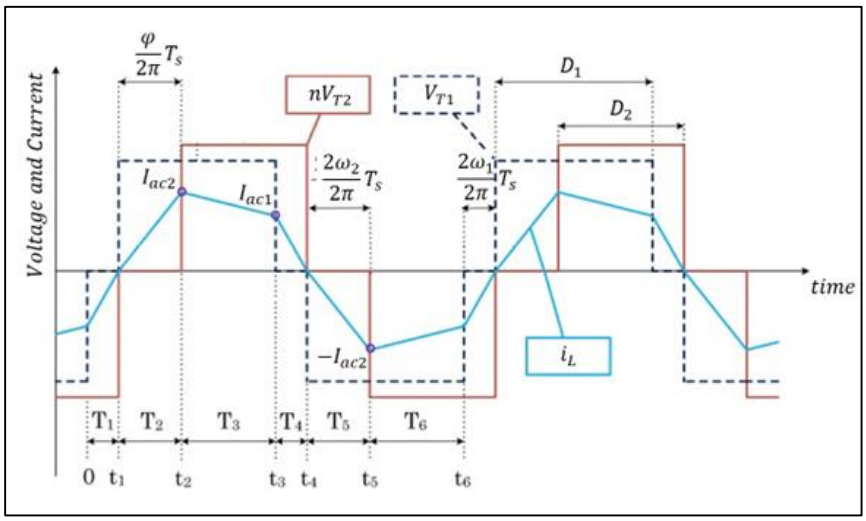

Figure 5 Primary and referred secondary transformer voltage and inductor current for the trapezoidal modulation

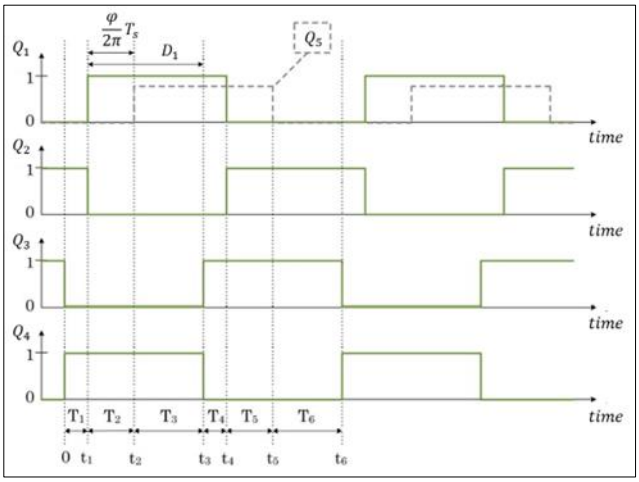

Figure 6 Switching signals for the gates Q_1 to Q_4

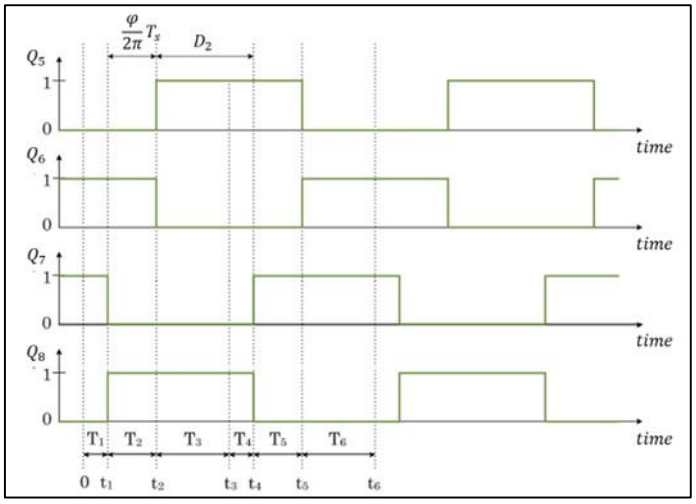

Figure 7 Switching signals for the gates Q_5 to Q_8

Table 2 Commutation sequence of switches for the Trapezoidal modulation

Q_1	Q_2	Q_3	Q_4	Q_5	Q_6	Q_7	Q_8	V_{T1}	nV_{T2}	Duration
0	1	0	0	0	1	1	0	0	$-nV_{T1}$	T_1
1	0	0	1	0	1	0	1	$+V_{T1}$	0	T_2
1	0	0	1	1	0	0	1	$+V_{T1}$	$+nV_{T1}$	T_3
1	0	1	0	1	0	0	1	0	$+nV_{T1}$	T_4
0	1	1	0	1	0	1	0	$-V_{T1}$	0	T_5
0	1	1	0	0	1	1	0	$-V_{T1}$	$-nV_{T1}$	T_6

2.3. Triangular Modulation

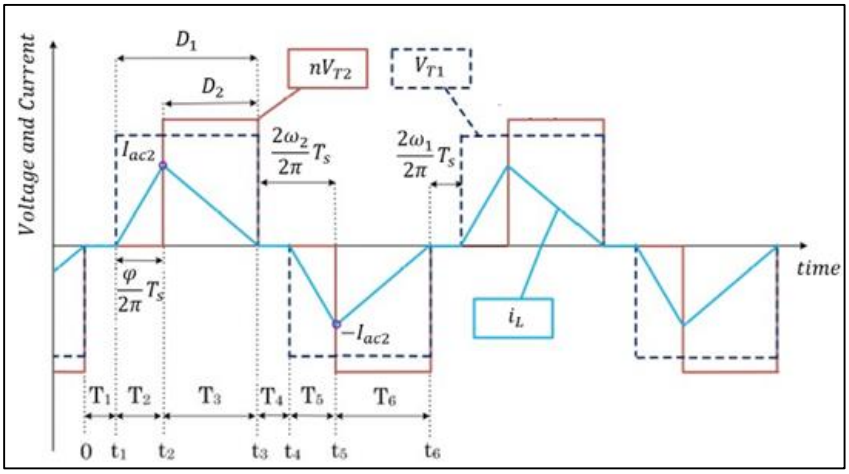

Figure 8 Primary and referred secondary transformer voltage and inductor current for the triangular modulation

The triangular modulation is a special case of a trapezoidal modulation. The current ramped to achieve zero-current switching on one full bridge. This modulation is only possible, if the two input voltages V_{in} and V_o are different [26]. But if one of the two voltages is equal to zero, this method cannot be used. The variables for controlling the power flow are the phase-shift angle between primary and secondary transformer voltage as well as a change in duty ratio of these

voltages [27]. In distinction from the trapezoidal modulation scheme, in the Triangular modulation features two time periods during which both square voltages V_{T1} and nV_{T2} are zero. This results in two-time intervals with zero inductor current i_L as can be seen in Figure 8. There are eight commutation states of the power switches to achieve the trapezoidal modulation method which are presented in Figures 9 and 10 and the commutation sequence of switches are tabulated in Table 3.

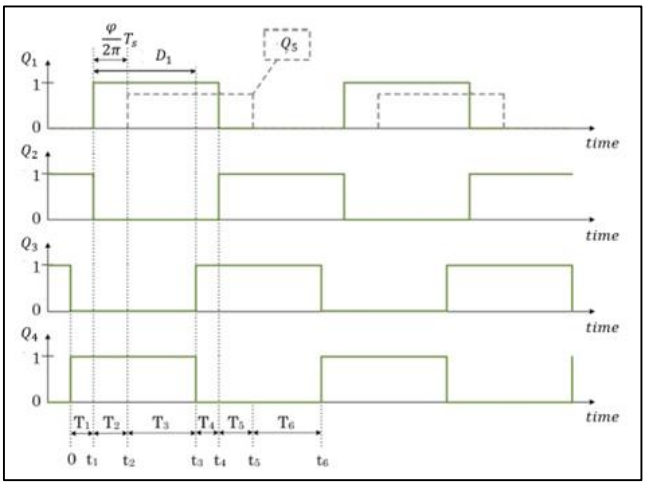

Figure 9 Switching signals for the gates Q_1 to Q_4

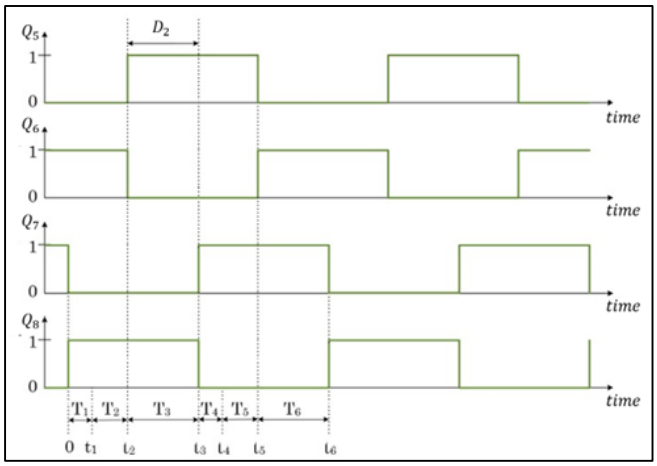

Figure 10 Switching signals for the gates Q_5 to Q_8

Table 3 Commutation sequence of switches for the Triangular modulation

Q_1	Q_2	Q_3	Q_4	Q_5	Q_6	Q_7	Q_8	V_{T1}	nV_{T2}	*Duration*
0	1	0	1	0	1	0	1	0	0	T_1
1	0	0	1	0	1	0	1	$+V_{T1}$	0	T_2
1	0	0	1	1	0	0	1	$+V_{T1}$	$+nV_{T1}$	T_3
1	0	1	0	1	0	1	0	0	0	T_4
0	1	1	0	1	0	1	0	$-V_{T1}$	0	T_5
0	1	1	0	0	1	1	0	$-V_{T1}$	$-nV_{T1}$	T_6

3. Simulation results and discussion

The model of the DAB can be built in PSIM®. Parameters that are defined in the Simulation Parameter Initialization dialogue in PSIM® are given in Table 4. The definition of certain parameters will be explained in the following sections. A schematic of the PSIM® model is presented in Figure 11 and 12.

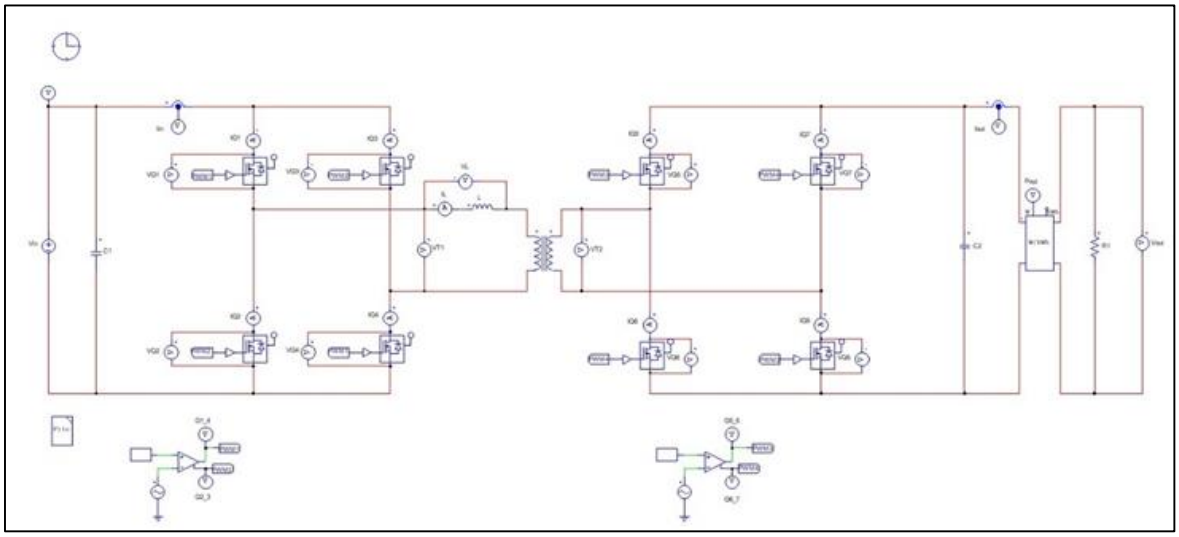

Figure 11 Schematic of the DAB model in PSIM® for the SPS Modulation

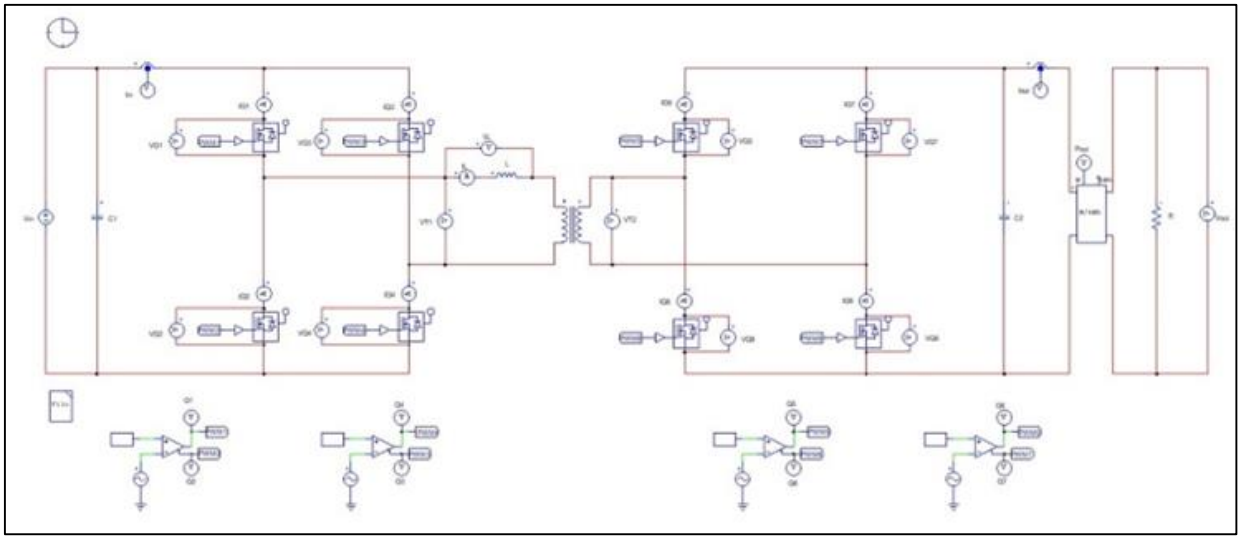

Figure 12 Schematic of the DAB model in PSIM® for the Trapezoidal Modulation

After modeling the Dual-Active-Bridge and the two modulation schemes in PSIM®, we can now analyze and compare these two modulation methods. The output voltage *Vo* ranges between 250 V and 400 V, with the load case considered at full load for the respective output voltage. Each modulation scheme is simulated individually, and the results of each case are compared and evaluated based on RMS inductor current, total losses of the semiconductor switches, overall efficiency, switching losses, and soft-switching range.

Table 4 Simulation Parameter Initialization

Specifications	Parameter	Value
Input Voltage	V_{in}	400 V
Output Voltage	V_o	250 V - 400 V
Maximum Input Power	P_{in_max}	1.8 KW - 3.1 KW
Switching Frequency	f_s	100 KHz
Primary Number of Turns	N_1	1
Secondary Number of Turns	N_2	1
Turn Ratio	n	1
On-Resistance $\boldsymbol{R_{DS(on)}}$	R_{on_LV}	35 mΩ
On-Resistance $\boldsymbol{R_{DS(on)}}$	R_{on_HV}	35 mΩ
Leakage Inductance	L	43 μH
Output Capacitance	C	470 μF

3.1. Single-Phase-Shift Modulation

In Figures 13 and 14, the DAB is subjected to an output voltage ranging between 250 V and 400 V. All waveforms exhibit the theoretically expected behavior illustrated in Figure 3. It is evident that the current slope increases as the output voltage decreases, and the current value decreases accordingly due to the reduction in maximum output power.

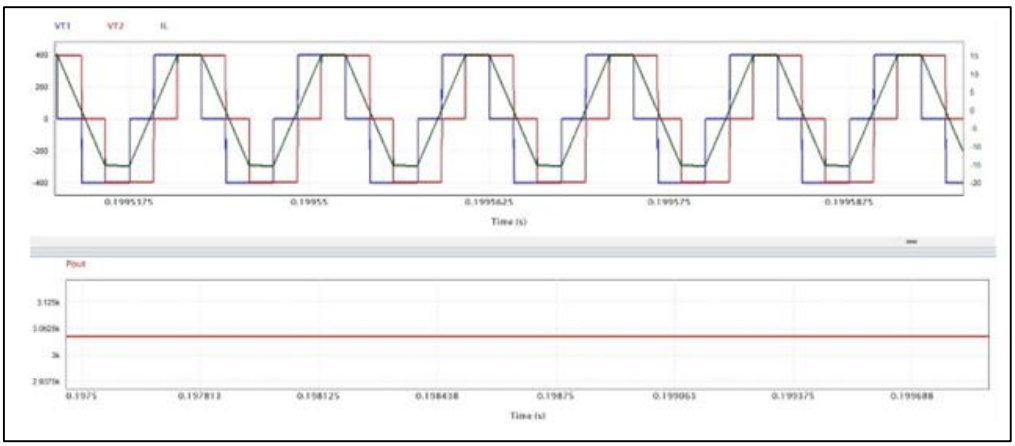

Measure

	X1	X2	Δ	Average	RMS
Time	2.99909e-001	2.99919e-001	1.00254e-005		
VT1	3.91731e+002	3.91731e+002	-1.44413e-004	1.94896e+000	3.91830e+002
VT2	3.90774e+002	3.90774e+002	1.09090e-004	1.94417e+000	3.90746e+002
IL	9.58509e+000	9.58559e+000	4.97009e-004	5.02876e-002	8.91089e+000

Measure

	X1	X2	Δ	Average	RMS
Time	2.99733e-001	2.99752e-001	1.83078e-005		
Pout	2.95954e+003	2.95954e+003	1.57221e-005	2.95954e+003	2.95954e+003

Figure 13 Primary and referred secondary transformer voltage $\boldsymbol{V_{T1}}$ and $\boldsymbol{nV_{T2}}$ and respective inductor current $\boldsymbol{i_L}$ and the output power at $\boldsymbol{V_o = 400\ V}$ with SPS Modulation

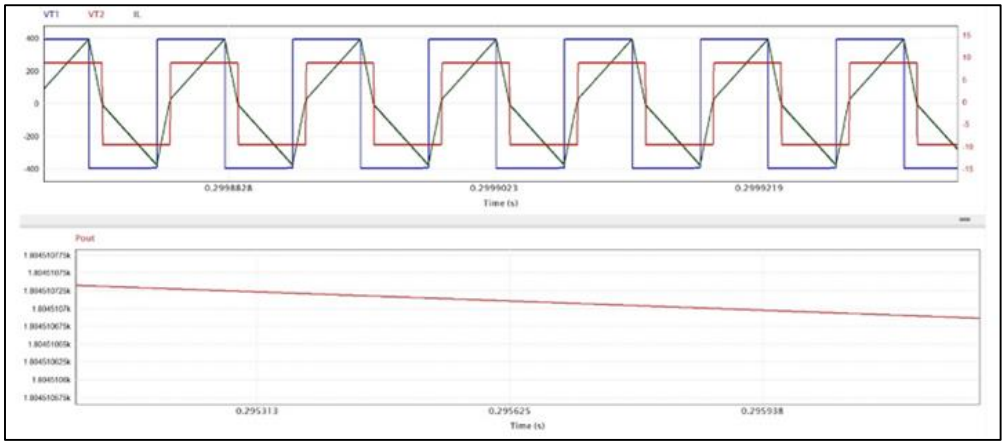

Measure

	X1	X2	Δ	Average	RMS
Time	2.99889e-001	2.99899e-001	1.01357e-005		
VT1	3.95336e+002	3.95304e+002	-3.21760e-002	5.84228e+000	3.94986e+002
VT2	2.50123e+002	2.50122e+002	-1.69187e-003	3.69697e+000	2.49369e+002
IL	1.08918e+000	1.54744e+000	4.58251e-001	1.95693e-002	8.19101e+000

Measure

	X1	X2	Δ	Average	RMS
Time	2.95311e-001	2.95367e-001	5.59006e-005		
Pout	1.80451e+003	1.80451e+003	-2.28790e-006	1.80451e+003	1.80451e+003

Figure 14 Primary and referred secondary transformer voltage $\boldsymbol{V_{T1}}$ and $\boldsymbol{nV_{T2}}$ and respective inductor current $\boldsymbol{i_L}$ and the output power at $\boldsymbol{V_o = 250\ V}$ with SPS Modulation

3.2. Trapezoidal Modulation

The waveforms from the simulation of the trapezoidal modulation exhibit the expected behaviour outlined in Figures 15 and 16. Like SPS Modulation, the current value decreases as the load decreases. According to the equations in the Trapezoidal Modulation section, the zero-voltage widths ω_1 and ω_2 decrease with a decreasing phase-shift angle, while the duty cycles increase. Furthermore, the current slope alternates in the third time interval when (V_{in}−nV_o) is applied, depending on the relationship between V_{in} and nV_o, as described in the Trapezoidal Modulation section.

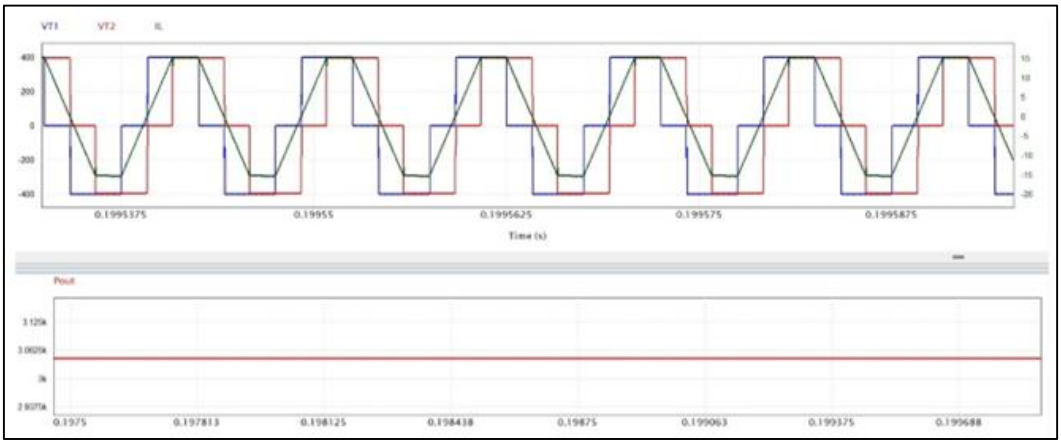

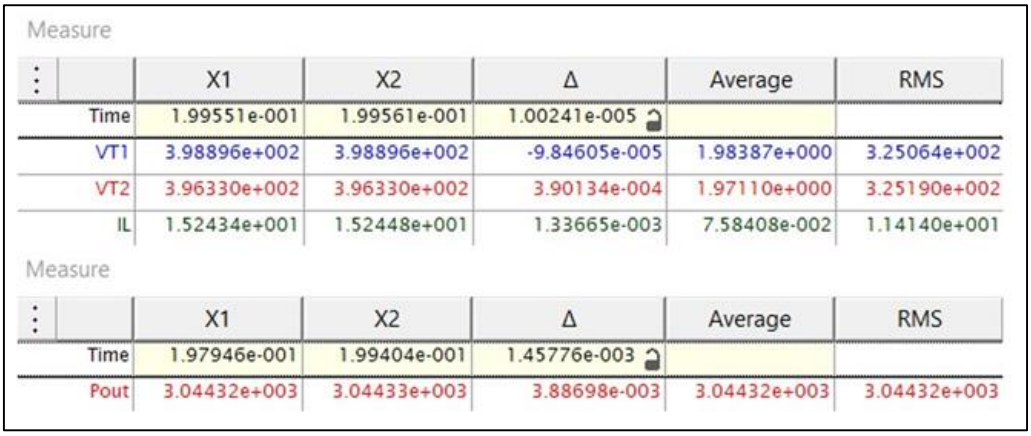

Measure

	X1	X2	Δ	Average	RMS
Time	1.99551e-001	1.99561e-001	1.00241e-005		
VT1	3.98896e+002	3.98896e+002	-9.84605e-005	1.98387e+000	3.25064e+002
VT2	3.96330e+002	3.96330e+002	3.90134e-004	1.97110e+000	3.25190e+002
IL	1.52434e+001	1.52448e+001	1.33665e-003	7.58408e-002	1.14140e+001

Measure

	X1	X2	Δ	Average	RMS
Time	1.97946e-001	1.99404e-001	1.45776e-003		
Pout	3.04432e+003	3.04433e+003	3.88698e-003	3.04432e+003	3.04432e+003

Figure 15 Primary and referred secondary transformer voltage $\boldsymbol{V_{T1}}$ and $\boldsymbol{nV_{T2}}$ and respective inductor current $\boldsymbol{i_L}$ and the output power at $\boldsymbol{V_o = 400\ V}$ with Trapezoidal Modulation

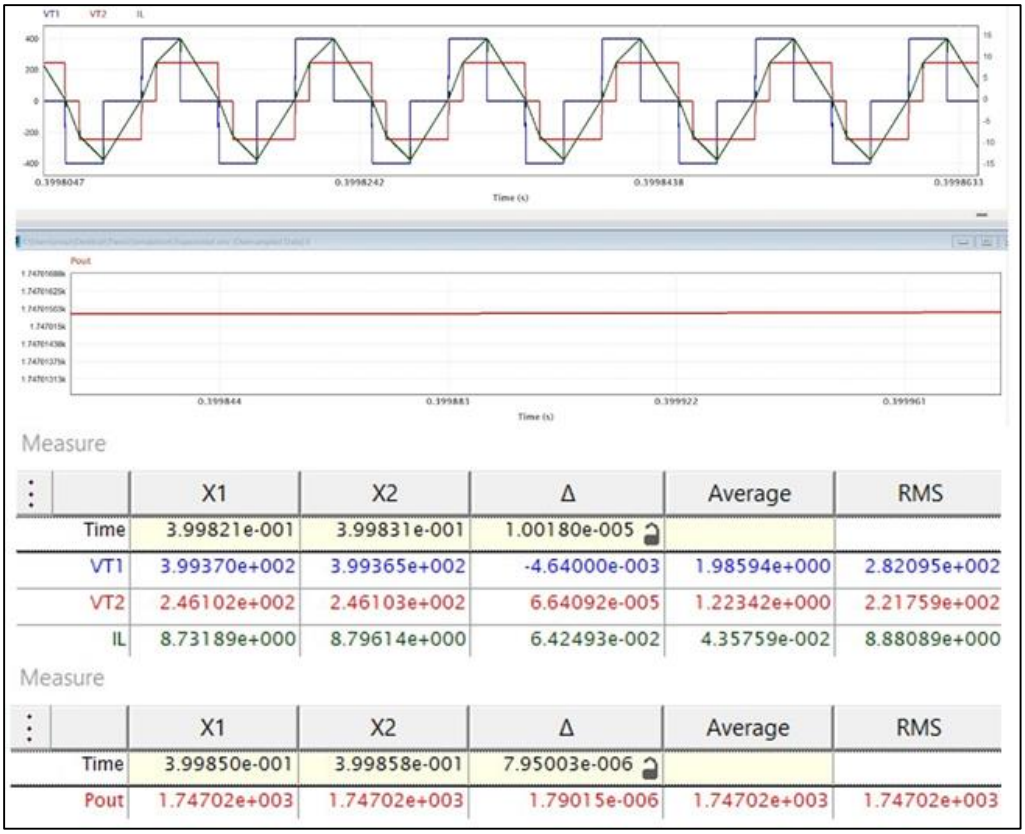

Measure

	X1	X2	Δ	Average	RMS
Time	3.99821e-001	3.99831e-001	1.00180e-005		
VT1	3.99370e+002	3.99365e+002	-4.64000e-003	1.98594e+000	2.82095e+002
VT2	2.46102e+002	2.46103e+002	6.64092e-005	1.22342e+000	2.21759e+002
IL	8.73189e+000	8.79614e+000	6.42493e-002	4.35759e-002	8.88089e+000

Measure

	X1	X2	Δ	Average	RMS
Time	3.99850e-001	3.99858e-001	7.95003e-006		
Pout	1.74702e+003	1.74702e+003	1.79015e-006	1.74702e+003	1.74702e+003

Figure 16 Primary and referred secondary transformer voltage $\boldsymbol{V_{T1}}$ and $\boldsymbol{nV_{T2}}$ and respective inductor current $\boldsymbol{i_L}$ and the output power at $\boldsymbol{V_o = 250\ V}$ with Trapezoidal Modulation

4. Comparison of Single-Phase-Shift and Trapezoidal Modulation:

4.1. RMS Inductor Current

In the following, Figure 17, the course of the RMS inductor current is depicted for the different output voltages in full load condition. It can be noted that by decreasing the output voltage, the current value decreases with decreasing load. It is apparent that, the Single-Phase-Shift Modulation presents higher RMS current values than the Trapezoidal Modulation.

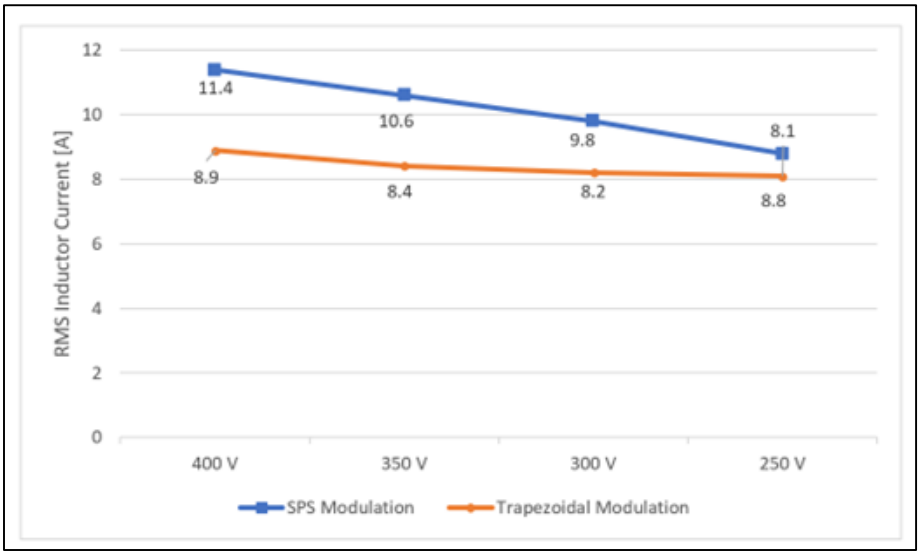

Figure 17 RMS inductor current at different output voltage in both SPS Modulation and Trapezoidal Modulation

4.2. Total Losses and Efficiency

Figure 18 displays the total losses, while Figure 19 illustrates the corresponding efficiencies of the constructed model. These losses comprise switching losses and conduction losses of the semiconductor switches. It's evident that total losses decrease with a decrease in output voltage and consequently with a decrease in load. As anticipated from the RMS current trends, the total losses in Trapezoidal Modulation are slightly larger than those in Single-Phase Shift Modulation. Consequently, it's observable in Figure 19 that SPS Modulation yields better efficiency than Trapezoidal Modulation. For lower output voltage values, the figures indicate that despite having fewer total losses, efficiency is reduced. This outcome can be elucidated by examining the distribution of switching and conduction losses at various load levels, as presented in the subsequent section.

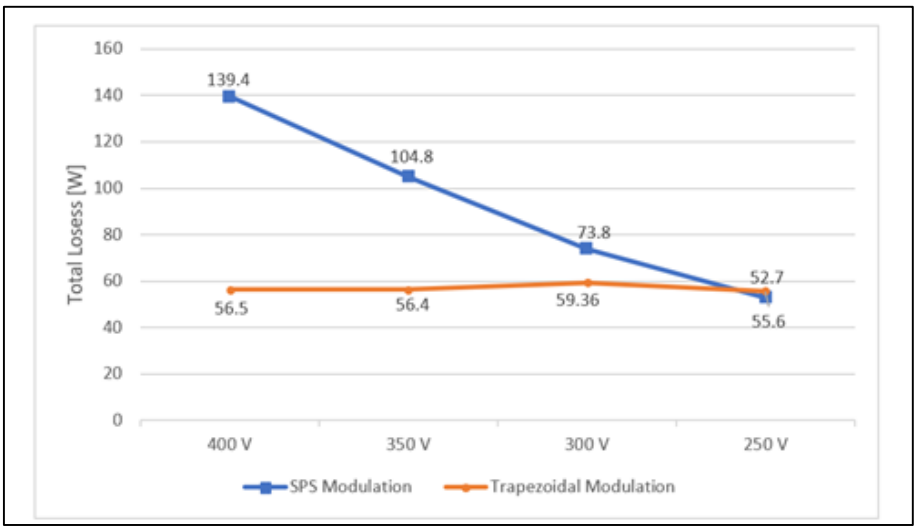

Figure 18 Total losses at different output voltages and MOSFET switches

Overall, the efficiency of the constructed DAB controlled via SPS Modulation ranges from 95.48% to 96.97%, depending on the load and voltage conditions. In contrast, if the control is executed through the Trapezoidal Modulation scheme, the efficiency ranges from 96.91% to 98.17%.

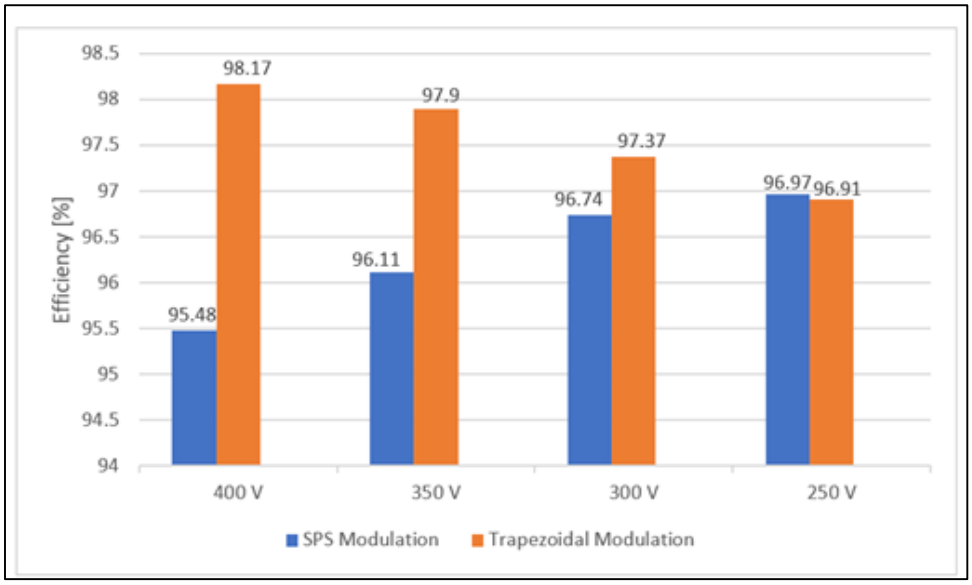

Figure 19 Efficiency at different output voltages and MOSFET switches

4.3. Switching Behaviour

Based on the simulations depicted in Figures 20 and 21, which illustrate the switching behaviors in SPS Modulation and Trapezoidal Modulation when *Vo*=400 V, we can observe the switching behavior consistent with our previous discussions in both modulation schemes.

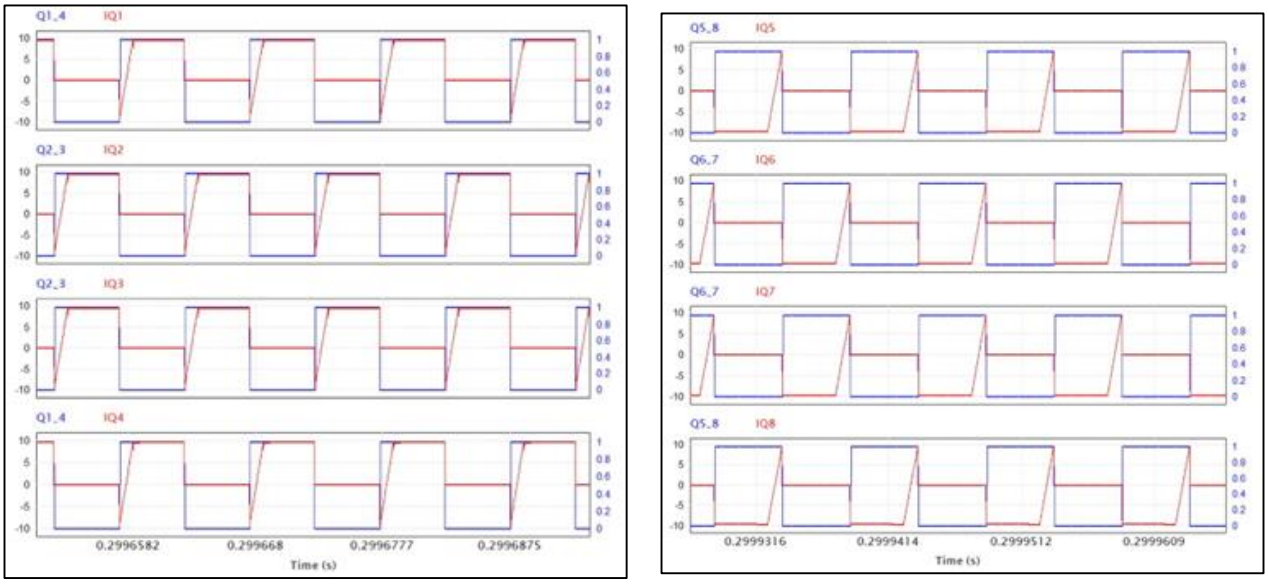

(a) (b)

Figure 20 Switching behavior for: (a): $\boldsymbol{Q_1}$ to $\boldsymbol{Q_4}$ (b): $\boldsymbol{Q_5}$ to $\boldsymbol{Q_8}$ in the SPS Modulation in full load when $\boldsymbol{V_o = 400\ V}$

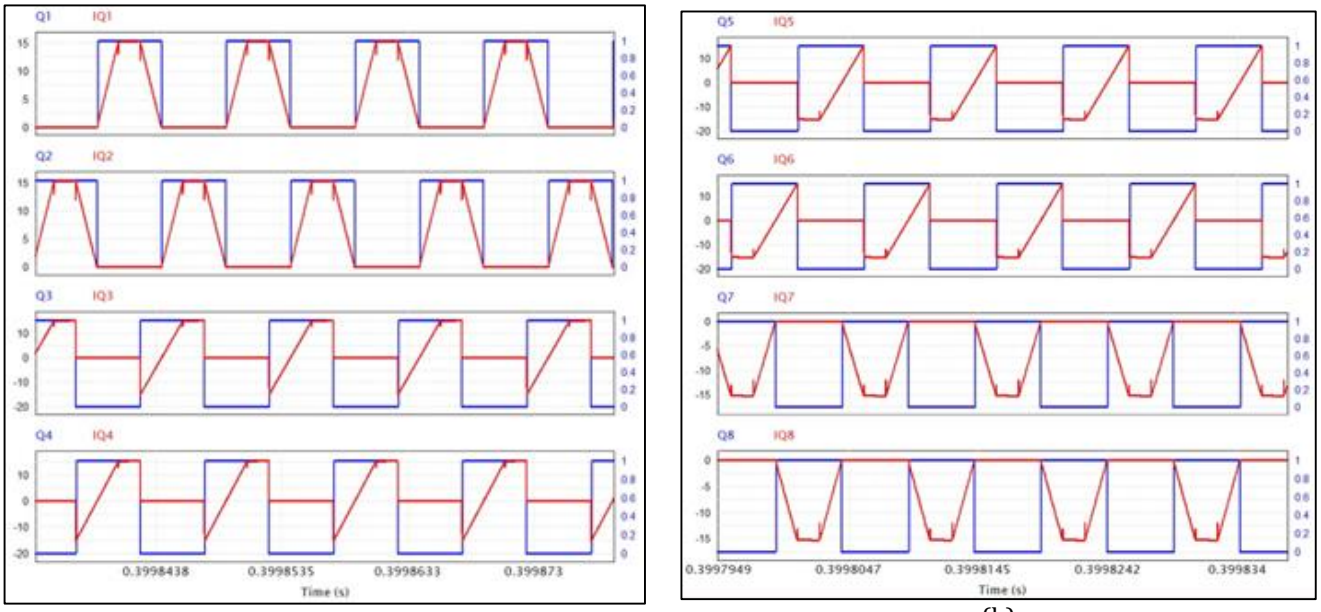

(a) (b)

Figure 21 Switching behaviour for: (a): Q_1 to Q_4 (b): Q_5 to Q_8 in the Trapezoidal Modulation in full load when $V_o = 400\ V$.

4.4. Switching Losses

Generally, it is evident that the percentage shares of switching losses relative to total losses increase with decreasing load. This is because the current, and consequently, the absolute value of conduction losses decrease. Additionally, SPS Modulation and Trapezoidal Modulation exhibit different characteristics regarding soft switching, as discussed in previous sections. Based on these observations, Trapezoidal modulation is expected to demonstrate a lower proportion of switching losses compared to SPS modulation. This assumption is supported by Figure 22, where at Vo=250 V, the switching losses with Trapezoidal Modulation account for only around half of the switching losses in SPS Modulation. This behavior is reflected in the overall efficiency at all loads. Moreover, as shown in Figure 17, the RMS inductor current in Trapezoidal Modulation is consistently smaller than in SPS Modulation. This results in smaller absolute values of conduction losses in Trapezoidal Modulation compared to SPS Modulation.

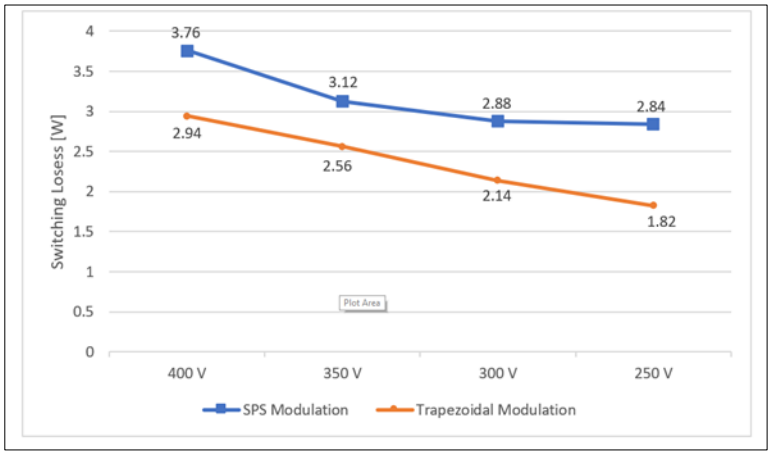

Figure 22 Total Switching Losses in both SPS Modulation and Trapezoidal Modulation in full load when the output voltage varies

5. Conclusion

The research confirms that integrating GaN technology into DAB-based on-board battery chargers significantly enhances the performance of charging systems in electric and hybrid vehicles. The use of GaN results in higher efficiency

and better thermal management compared to traditional Silicon-based systems. The simulations demonstrate that both Single-Phase-Shift and Trapezoidal Modulation methods can be effectively implemented, with Trapezoidal Modulation providing slightly better efficiency under varying load conditions. This study not only highlights the technical benefits of using GaN in DAB configurations but also suggests its practical implications for future automotive designs, promoting the adoption of more energy-efficient and high-performance charging solutions in the transportation sector. Future work could explore the long-term durability and cost-effectiveness of GaN-based systems to further validate their commercial viability.

Compliance with ethical standards

Disclosure of conflict of interest

The authors declare that they have no known competing financial interests or personal relationships that could have appeared to influence the work reported in this paper.

References

[1] Di Cataldo A, Giordano A, Eivazi H, Aiello G, Gennaro F. Performance Evaluation of GaN Technology on MultiLevel Inverters for Electric Traction Systems.

[2] Chilakalapudi G, Kumar A. Optimal reactive power control for dual-active-bridge converter using improved dual-phase-shift modulation strategy for electric vehicle application. International Journal of Circuit Theory and Applications. 2023 Mar;51(3):1204-23.

[3] Taghavi H, El Shafei A, Nasiri A. Liquid Cooling System for a High Power, Medium Frequency, and Medium Voltage Isolated Power Converter. In2023 12th International Conference on Renewable Energy Research and Applications (ICRERA) 2023 Aug 29 (pp. 405-413). IEEE.

[4] Mirtchev AV, Tatakis EC. Design methodology based on dual control of a resonant dual active bridge converter for electric vehicle battery charging. IEEE Transactions on Vehicular Technology. 2022 Jan 13;71(3):2691-705.

[5] Guennouni N, Chebak A, Machkour N. Optimal Dual Active Bridge DC-DC Converter Operation with Minimal Reactive Power for Battery Electric Vehicles Using Model Predictive Control. Electronics. 2022 May 19;11(10):1621.

[6] Zayed O, Elezab A, Abuelnaga A, Narimani M. A dual-active bridge converter with a wide output voltage range (200-1000 v) for ultra-fast dc-connected ev charging stations. IEEE Transactions on Transportation Electrification. 2022 Dec 26.

[7] Bhuvela P, Taghavi H, Nasiri A. Design Methodology for a Medium Voltage Single Stage LLC Resonant Solar PV Inverter. In2023 12th International Conference on Renewable Energy Research and Applications (ICRERA) 2023 Aug 29 (pp. 556-562). IEEE.

[8] Aouiti A, Bacha F. Unidirectional Three Phase Dual Active Bridge DC-DC Converter Used in Electrical Vehicles. In2020 4th International Conference on Advanced Systems and Emergent Technologies (IC_ASET) 2020 Dec 15 (pp. 43-49). IEEE.

[9] Rafi MA, Bauman J. Optimal control of semi-dual active bridge DC/DC converter with wide voltage gain in a fast-charging station with battery energy storage. IEEE Transactions on Transportation Electrification. 2022 Apr 26;8(3):3164-76.

[10] Mohammadzadeh SF, Hadifar N, Rajabi A, Taheri M. A Novel Topology of Quasi-Resonant DC-DC Boost Converter for Electric Vehicle Charging Stations.

[11] Hadifar N, Ayanlou A. A Comparative Feasibility Study of Stand-Alone and Grid-Connected PV System for Residential Load: A Case Study in Iran. InE3S Web of Conferences 2021 (Vol. 239, p. 00008). EDP Sciences.

[12] Mohammadzadeh M, Hadifar N, Mohammadzadeh B. A sustainable PV-powered energy retrofit modelling to achieve net ZEB in churches: a simulation study for San Marcello Al Corso. International Journal of Exergy. 2021;36(2-4):191-207.

[13] Geri A, Gatta FM, Maccioni M, Dell'Olmo J, Carere F, Bucarelli MA, Poursoltan P, Hadifar N, Paulucci M. Distributed generation monitoring: a cost-effective Raspberry Pi-based device. In2022 2nd International Conference on Innovative Research in Applied Science, Engineering and Technology (IRASET) 2022 Mar 3 (pp. 1-6). IEEE.

[14] Geri A, Gatta FM, Maccioni M, Dell'Olmo J, Carere F, Bucarelli MA, Poursoltan P, Hadifar N, Paulucci M. A Low-Cost Smart Monitoring Device for Demand-Side Response Campaigns. InProceedings of Seventh International Congress on Information and Communication Technology: ICICT 2022, London, Volume 2 2022 Jul 27 (pp. 593-603). Singapore: Springer Nature Singapore.

[15] Biglo AH, Farhangi S, Iman-Eini H. A Novel Zero Voltage Transition soft-switching PWM Boost Converter with low voltage stress. In2021 12th Power Electronics, Drive Systems, and Technologies Conference (PEDSTC) 2021 Feb 2 (pp. 1-5). IEEE.

[16] Farzamkia S, Farhangi S, Iman-Eini H. Utilization of Soft-Switched Boost Converter for MPPT Application in Photovoltaic Single-Phase Grid-Connected Inverter. In2020 11th Power Electronics, Drive Systems, and Technologies Conference (PEDSTC) 2020 Feb 4 (pp. 1-6). IEEE.

[17] Capó-Lliteras M, Heredero-Peris D, Diaz-Gonzalez F, Llonch-Masachs M, Montesinos-Miracle D. Analytical Dead-Band Compensation for ZCS Modulation Applied to Hybrid Si-SiC Dual Active Bridge. IEEE access. 2020 Oct 2;8:181577-89.

[18] Kerachev L, Trinh TH, Lembeye Y, Crebier JC. Design and implementation of a highly integrated dual active bridge microconverter. IEEE Transactions on Power Electronics. 2015 Oct 26;31(8):5635-43.

[19] Rao JR, Venkateshwarlu S. Soft-switching dual active bridge converter-based bidirectional on-board charger for electric vehicles under vehicle-to-grid and grid-to-vehicle control optimization. Journal of Engineering and Applied Science. 2024 Dec;71(1):49.

[20] Agrawal A. Circulating power flow restricted operation of the isolated bi-directional dual-active bridge DC-DC converter for battery charging applications. Journal of Energy Storage. 2024 May 1;86:111123.

[21] Shahir FM, Aliasghari TP, Aberoumandazar M. Switching Correction of Direct Torque Control Method in order to Improve the Electrical Vehicle Performance Quality. In2021 International Symposium on Devices, Circuits and Systems (ISDCS) 2021 Mar 3 (pp. 1-4). IEEE.

[22] Abhijith N, TG SJ, John V. Minimum leakage inductance for soft-switching of dual-active half-bridge DC-DC converter. In2020 IEEE International Conference on Power Electronics, Drives and Energy Systems (PEDES) 2020 Dec 16 (pp. 1-6). IEEE.

[23] Zhang H, Isobe T. An improved charge-based method extended to estimating appropriate dead time for zero-voltage-switching analysis in dual-active-bridge converter. Energies. 2022 Jan 17;15(2):671.

[24] Wang C, Xiao Y, Zsurzsan G, Zhang Z. Artificial intelligence assisted parametric design by splitting inductance in dual active bridge converter. In2021 IEEE 12th Energy Conversion Congress & Exposition-Asia (ECCE-Asia) 2021 May 24 (pp. 554-561). IEEE.

[25] Khatua S, Kastha D, Kapat S. A dual active bridge derived hybrid switched capacitor converter based two-stage 48 V VRM. IEEE Transactions on Power Electronics. 2020 Dec 22;36(7):7986-99.

[26] Li L, Xu G, Xiong W, Liu D, Su M. An optimized DPS control for dual-active-bridge converters to secure full-load-range ZVS with low current stress. IEEE Transactions on Transportation Electrification. 2021 Aug 19;8(1):1389-400.

[27] Shahir FM, Aliasghari TP, Babaei E. Analysis of Self-Lift Luo Converter in DCM and Critical Inductance Calculation. In2021 International Symposium on Devices, Circuits and Systems (ISDCS) 2021 Mar 3 (pp. 1-4). IEEE.